

# Physical Layer Considerations for Wideband Cognitive Radio

Joel Goodman, Benjamin A. Miller, James Vian, Andrew Bolstad, Janani Kalyanam and Matthew Herman

**Abstract**—Next generation cognitive radios will benefit from the capability of transmitting and receiving communications waveforms across many disjoint frequency channels spanning hundreds of megahertz of bandwidth. The information theoretic advantages of multi-channel operation for cognitive radio (CR), however, come at the expense of stringent linearity requirements on the analog transmit and receive hardware. This paper presents the quantitative advantages of multi-channel operation for next generation CR, and the advanced digital compensation algorithms to mitigate transmit and receive nonlinearities that enable broadband multi-channel operation. Laboratory measurements of the improvement in the performance of a multi-channel CR communications system operating below 2 GHz in over 500 MHz of instantaneous bandwidth are presented.

## I. INTRODUCTION

Cognitive radio (CR) departs from the traditional approach to increase spectral efficiency and physical layer transmission. CRs search for open locations in the spectrum (white space) to communicate, while conventional communications systems operate in a predetermined fixed band [1]. Transmitting a waveform over multiple noncontiguous frequency channels with arbitrary bandwidth yields a more jam resistant and spectrally efficient waveform, and this significantly benefits CR.

As an example, consider the case of two cognitive radios employing different transmission strategies to exploit white space in a 200 MHz band. The first transmits all its power in a single 10 MHz band, while the second spreads the same total power across five noncontiguous 10 MHz bands. For this example, assume both CRs experience the hidden node problem [5]; the receiver sees interference 35 dB greater than the signal power in half of the available 10 MHz bands, but this interference is not detected by either transmitter. In addition, the receiver experiences additive white Gaussian noise (AWGN) across the entire band. It is well known that there is an information-theoretic advantage to spreading a waveform over a wider bandwidth since capacity increases linearly with increasing bandwidth but only logarithmically with increasing signal-to-noise ratio (SNR) [3]. In addition, as shown in Fig. 1, the transmitter which spreads power over five bands also enjoys a clear advantage over the single band transmitter when there is a high probability of interference.

This work is sponsored by the department of the Air Force under contract FA8721-05-C-0002. Opinions, interpretations, conclusions and recommendations are those of the author and are not necessarily endorsed by the United States Government.

Joel Goodman, Benjamin Miller, James Vian and Andrew Bolstad are with MIT Lincoln Laboratory, Lexington, MA, 02420 USA (e-mail: {jgoodman, bamiller, vian, andrew.bolstad}@ll.mit.edu).

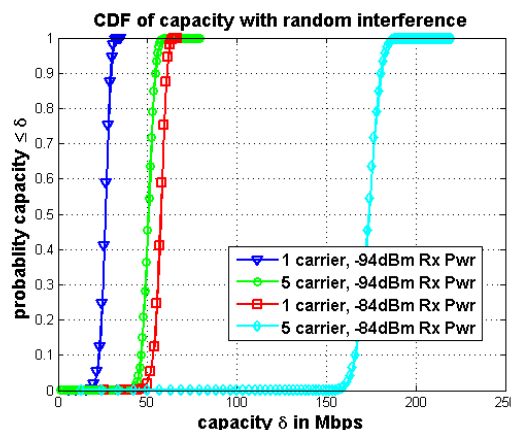


Fig. 1. Cumulative distribution of the capacity of a single carrier vs. five carrier transmitter for two receiver power levels.

There are, however, significant obstacles to deploying agile wideband systems that operate on spectrally segmented waveforms. Transmitters generate both adjacent channel interference (ACI) and in band distortion (e.g., loss of sub-carrier orthogonality) due to nonlinear mixing of spectrally segmented waveforms [4]. The simplest approach to linearizing a wideband transmitter is to use a highly linear class A or AB power amplifier in combination with output power backoff (OBO). This is a very unattractive option for systems with size, weight and power (SWaP) constraints. For example, a class AB amplifier with a 10% power added efficiency (PAE) and 5 dB OBO would generate roughly 50 times<sup>1</sup> more power as heat than actual transmit power. On the receiver side, limited dynamic range can mask or falsely indicate the presence of a signal. Strong out-of-band signals can generate nonlinear distortions that inadvertently jam signals in bands of interest. This can prevent CRs from detecting white space or demodulating a waveform with the fidelity needed to achieve a target bit error rate (BER).

In this paper we present both the mathematics and measured performance results of wideband transmitter and receiver digital linearization operating on spectrally segmented waveforms, and its effect on CR performance. Our approach to linearization divides the full multi-dimensional coefficient space of a Volterra series [6] using cube coefficient subspaces (CCS) [7] and then identifies only a small CCS subset for digital

<sup>1</sup>The factor of 50 represents measurements made in our laboratory and accounts for the effect of an amplifier operating at 1 dB compression. Not accounting for the effect of compression would mean  $70 \times$  more heat is generated than actual transmit power.

linearization. The rest of this paper is organized as follows. In Section II, we develop the mathematics of CCS for constructing digital transmit and receive linearization. In Section III we compare the measured linearization performance of CCS in CR applications, and in Section IV we conclude with a brief summary.

## II. DERIVING A NONLINEAR DIGITAL COMPENSATION ARCHITECTURE

Active and mixed signal RF (and optical) devices exhibit nonlinear behavior that is manifest by a state dependent nonlinear transfer function relating input to output. State dependence is generally an artifact of wide band operation, where the current output sample is not only related nonlinearly to the current input sample, but by the nonlinear combination of the  $M$  preceding input samples. In general, developing nonlinear digital compensation (NDC) for active nonlinear devices is a three step process. In the first step, we send several training sets through the transmitter or receiver with the goal of exciting all of the nonlinear modalities [8]. Next, we choose a basis for representing the nonlinear response. We have been successful using polynomial bases, although other bases could be used [9]. Lastly, we solve a sequential optimization problem to derive NDC (Section II-D). In the following subsections the symbol  $x(n)$  corresponds to the  $n$ th digital input symbol to the transmitter's predistorter, and  $y(n)$  its output.

### A. Polynomial Modeling Overview

We establish a polynomial NDC architecture beginning with the finite order, finite memory complex baseband Volterra series derived in [6]:

$$y(n) = \sum_{\substack{p=1 \\ p \text{ odd}}}^P u_p[x(n)] \quad (1)$$

where

$$u_p[x(n)] = \sum_{m_1=0}^{M-1} \cdots \sum_{m_p=0}^{M-1} h_p(m_1, \dots, m_p) \times \prod_{k=1}^{\lceil p/2 \rceil} x(n - m_k) \prod_{\ell=\lceil p/2 \rceil+1}^p x^*(n - m_\ell), \quad (2)$$

In (2) the superscript  $*$  represents the complex conjugate operator,  $\lceil \cdot \rceil$  represents the smallest integer no less than its argument, and  $x(n)$  and  $y(n)$  are the respective input and output signals of the transmitter or receiver at baseband. Each term  $u_p[x(n)]$  in the series has polynomial order  $p$  and memory depth  $M$ . The coefficients  $h_p(m_1, \dots, m_p)$  are known as the Volterra kernels. By Weierstrass' theorem [10], a Volterra series with sufficiently high polynomial order and sufficient memory can model any nonlinearity with arbitrary precision.

We can recast equations (1) and (2) in matrix form. Let the discrete time variable  $n$  be in the set  $\{0, 1, 2, \dots, N-1\}$  and assume that the input sequence is 0 for all times  $n < 0$ . Hence, the input sequence  $x(n)$  can be represented by the vector

$$\mathbf{x} = [x(0) \ x(1) \ x(2) \ \cdots \ x(N-1)]^T \quad (3)$$

and the output sequence  $y(n)$  is given by the vector

$$\mathbf{y} = [y(0) \ y(1) \ y(2) \ \cdots \ y(N-1)]^T. \quad (4)$$

Likewise, we can write the Volterra kernels as one long coefficient vector  $\mathbf{h}$  given by

$$\mathbf{h} = \underbrace{[h_1(0) \ \cdots \ h_1(M-1)]}_{\text{First Order Kernel}} \underbrace{[h_3(0, 0, 0) \ \cdots \ h_3(M-1, M-1, M-1)]}_{\text{Third Order Kernel}} \underbrace{\cdots \ h_p(M-1, \dots, M-1)]^T}_{\text{Higher Order Kernels}} \quad (5)$$

Each coefficient is associated with a nonlinear combination of shifted values of the input signal  $x(n)$  in (2), which can be written as a column vector in exactly the same way as (3) and (4). We can put all of these column vectors into a nonlinear convolution matrix  $\mathbf{X}$  to write the entire complex baseband Volterra series as  $\mathbf{y} = \mathbf{X}\mathbf{h}$ .

### B. Cube Coefficient Subspaces

In order to make the Volterra series approach more efficient, we introduce the notion of coefficient subspaces, which provides a consistent method for dividing the full multidimensional coefficient spaces  $h_p(m_1, \dots, m_p)$  for each  $u_p[x(n)]$  into smaller pieces called processing elements that each contain only a small subset of the coefficients. The NDC architecture then consists of the sum of the outputs of a set of processing elements (of heterogeneous polynomial order) that have been identified to give a more compact model, as discussed in Section II-D.

Small sets of processing elements is the motivation behind the cube coefficient subspaces (CCS), which break the full Volterra kernel up into small nonlinear filters of arbitrary dimension and polynomial order [12]. Geometrically, a  $p$ th order,  $d$ -dimensional ( $d \leq p$ ) CCS component corresponds to a  $d$ -dimensional hypercube within the full  $p$ th order Volterra kernel (see Fig 2). The output of a CCS processing element is given by

$$y_{\text{CCS}}^{(p,d)}(n; \alpha_1, \dots, \alpha_p) = \sum_{m_1=0}^{M-1} \cdots \sum_{m_d=0}^{M-1} h_p(m_1 + \alpha_1, \dots, m_d + \alpha_d) \times \prod_{k=1}^{\lceil d/2 \rceil} x(n - m_k - \alpha_k) \prod_{\ell=\lceil d/2 \rceil+1}^d x^*(n - m_\ell - \alpha_\ell) \times \prod_{\hat{k}=d+1}^{d+\lceil \frac{p-d}{2} \rceil} x(n - \alpha_{\hat{k}}) \prod_{\hat{\ell}=d+\lceil \frac{p-d}{2} \rceil+1}^p x^*(n - \alpha_{\hat{\ell}}), \quad (6)$$

where the  $\alpha_i$  for  $i = 1, \dots, p$  are again fixed integer delays that determine the location of the CCS component within the full Volterra kernel. To further generalize CCS, we also designed a diagonal analog, the diagonal cube coefficient subspaces (CCS-D). In this case, a  $p$ th order,  $d$ -dimensional ( $d \leq p$ )

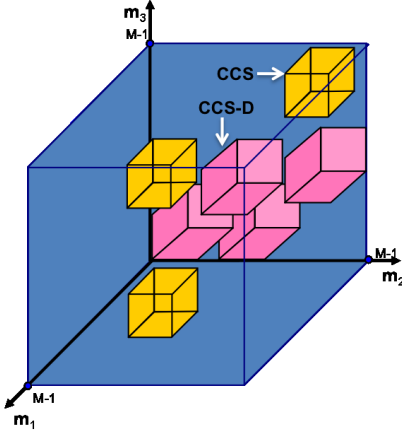


Fig. 2. Illustration of the geometry of a CCS model. The yellow hypercubes are third order, 3D CCS processing elements and the pink parallelepipeds are third order, 3D CCS-D processing elements. The model consists of all 7 components, which is just a small subset of the full third order Volterra kernel in blue.

CCS-D processing element has output given by

$$\begin{aligned}
 y_{\text{CCS-D}}^{(p,d)}(n; \alpha_1, \dots, \alpha_p) = & \sum_{m_1=0}^{M-1} \dots \sum_{m_d=0}^{M-1} h_p(m_1 + \alpha_1, \dots, m_d + m_1 + \alpha_d) \times \\
 & x(n - m_1 - \alpha_1) \prod_{k=2}^{\lceil d/2 \rceil} x(n - m_k - m_1 - \alpha_k) \times \\
 & \prod_{\ell=\lceil d/2 \rceil+1}^d x^*(n - m_\ell - m_1 - \alpha_\ell) \prod_{\hat{k}=d+1}^{d+\lceil \frac{p-d}{2} \rceil} x(n - m_1 - \alpha_{\hat{k}}) \times \\
 & \prod_{\hat{\ell}=d+\lceil \frac{p-d}{2} \rceil+1}^p x^*(n - m_1 - \alpha_{\hat{\ell}}).
 \end{aligned} \quad (7)$$

A  $d$ -dimensional CCS-D processing elements corresponds to a small parallelepiped of dimension  $d$  within the full  $p$ th order Volterra kernel. For the most flexible models, we use both CCS and CCS-D components. A notional graphic of the geometry of the  $p$ th order CCS/CCS-D coefficient space ( $h_p(\cdot)$ ) is shown in Figure 2.

### C. Other Pruned Volterra Methods

In addition to the coordinate system/coefficient subspace approach outlined in Section II-B, there are two simplifications of the complex baseband Volterra series, the memory polynomial (MP) [13] and generalized memory polynomial (GMP) [14], that have been used primarily as polynomial predistorters to invert transmitter nonlinearities with memory. We repeat their structures here for completeness. The output of a memory polynomial model has the form

$$y_{\text{MP}}(n) = \sum_{\substack{p=1 \\ p \text{ odd}}}^P \sum_{m=0}^{M-1} h_p(m) x(n-m) |x(n-m)|^{p-1}. \quad (8)$$

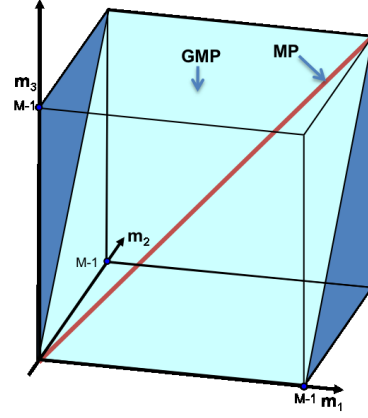


Fig. 3. Illustration of the geometry of the third order MP (red line) and GMP (light blue plane) coefficient space  $h_p(m)$ .

The generalized memory polynomial is given by

$$y_{\text{GMP}}(n) = \sum_{\substack{p=1 \\ p \text{ odd}}}^P \sum_{m_1=0}^{M-1} \sum_{m_2=0}^{M-1} h_p(m_1, m_2) x(n-m_1) |x(n-m_2-m_1)|^{p-1}. \quad (9)$$

Note that both MP and GMP are a subsets of CCS, restricting the space over which an NDC architecture can be identified. The MP assumes that all of the relevant terms of the complex baseband Volterra series lie along the main diagonals of the kernels, whereas the GMP gives some additional flexibility by also allowing us to consider some off-diagonal terms as well. The geometry of both MP and GMP are illustrated in 3.

### D. Model Identification

Assume we excite the transmitter or receiver with a set of  $K$  excitation sequences  $x_1(n), x_2(n), \dots, x_K(n)$  and collect the corresponding outputs  $y_1(n), y_2(n), \dots, y_K(n)$ . We identify a model by solving (or approximately solving) the following optimization problem:

$$\min_{\mathbf{h}} \frac{1}{2} \|\mathbf{y} - \tilde{\mathbf{X}}\mathbf{h}\|_2^2 \quad \text{such that} \quad \|\mathbf{h}\|_0 \leq N, \quad (10)$$

where  $\|\mathbf{h}\|_0$  is the  $\ell_0$  quasinorm which counts the number of nonzero elements in the vector  $\mathbf{h}$ , and

$$\mathbf{y} = \begin{bmatrix} y_1 \\ \vdots \\ y_K \end{bmatrix} \quad \text{and} \quad \tilde{\mathbf{X}} = \begin{bmatrix} \tilde{\mathbf{X}}_1 \\ \vdots \\ \tilde{\mathbf{X}}_K \end{bmatrix}, \quad (11)$$

where  $\mathbf{y}_1, \dots, \mathbf{y}_K$  are the vectors of output sequence samples and  $\tilde{\mathbf{X}}_1, \dots, \tilde{\mathbf{X}}_K$  are the filtered nonlinear convolution matrices corresponding to each of the excitation sequences. Problem (10) finds a model of reasonable complexity that minimizes the mean-squared error (MSE) associated with representing the input/output relationship with the set of basis vectors in  $\tilde{\mathbf{X}}$ . To solve (10) we developed a computationally efficient identification method (see Fig. 4) that sequentially chooses a CCS/CCS-D architecture, although other methods are possible [11].

### Sequential Estimation for Architecture Identification

```

Initialize:  $\mathcal{P} = \emptyset$ 
Add Processing Elements:
while  $\varepsilon(\mathbf{y}, \mathcal{P}) \geq \delta$ 
    Do least squares:
     $p^* \leftarrow \arg \min_{p \in \mathcal{X}} \varepsilon(\mathbf{y}, \mathcal{P} \cup \{p\})$ 
     $\mathcal{P} \leftarrow \mathcal{P} \cup \{p^*\}, \mathcal{X} \leftarrow \mathcal{X} \cup \{p^*\}$ 

```

Fig. 4. Pseudocode for sequential estimation for architecture identification. We start with an empty set of processing elements and then sequentially add the candidate processing element from  $\mathcal{X}$  that works best in conjunction with the other processing elements already in the architecture until an MMSE threshold  $\delta$  is met. Alternatively, we could terminate the algorithm when the architecture contains some maximum number of processing elements.

The sequential estimation method for architecture identification begins with a large, user-defined set  $\mathcal{X}$  of candidate CCS/CCS-D processing elements (of heterogeneous orders) that is designed to span large portions of the full Volterra kernels. The objective is to find a significantly smaller set of processing elements  $\mathcal{P} \subset \mathcal{X}$ , i.e. with  $|\mathcal{P}| \ll |\mathcal{X}|$ , that minimizes the model MSE. Let

$$\varepsilon(\mathbf{y}, \mathcal{P}) = \left\| \mathbf{y} - \tilde{\mathbf{X}}_{\mathcal{P}} \mathbf{h} \right\|_2^2 \quad (12)$$

denote MSE, where  $\tilde{\mathbf{X}}_{\mathcal{P}} = [\tilde{\mathbf{X}}^{(\text{PE}_1)} \dots \tilde{\mathbf{X}}^{(\text{PE}_{|\mathcal{P}|})}]$ . For example, processing element  $i$  with  $p = 3$  and  $d = 2$  is formulated as

$$\tilde{\mathbf{X}}^{(\text{PE}_i)} = \begin{bmatrix} \tilde{\mathbf{X}}_1^{(\text{PE}_i)} \\ \vdots \\ \tilde{\mathbf{X}}_K^{(\text{PE}_i)} \end{bmatrix}, \quad (13)$$

with each column of  $\tilde{\mathbf{X}}^{(\text{PE}_i)}$  given by

$$\mathbf{x}(n - m_1 - \alpha_1) \circ \mathbf{x}^*(n - m_2 - \alpha_2) \circ \mathbf{x}(n - \alpha_3), \quad (14)$$

where  $\mathbf{x}(n)$  is an  $S \times 1$  vector, the symbol  $\circ$  is the Hadamard product representing element wide multiplication,  $m_1$  and  $m_2$  vary independently from 0 to  $M - 1$ , and  $S$  is the number of samples in the excitation sequence. The pseudocode for sequentially selecting processing elements to construct a model is given in Fig. 4. We note that the total number of processing elements  $|\mathcal{X}|$ , can be adjusted according to computational considerations. Given sufficient computational resources, we can start with a set of candidate processing elements that, when taken together, comes close to approximating the full complex baseband Volterra series. Furthermore, it gives us the flexibility to control the computational complexity of the model. Its main disadvantage is that it involves a sequential search which is not guaranteed to find a theoretically optimal solution. Despite its greedy nature, this method performs well in practice.

### III. MEASURED RESULTS

To test the efficacy of digital compensation in a CR scenario using CCS, we developed the Combat Adaptive Radio Testbed (CART) pictured in Fig. 5. The general requirements for CART were to synthesize arbitrary waveforms spanning 1250

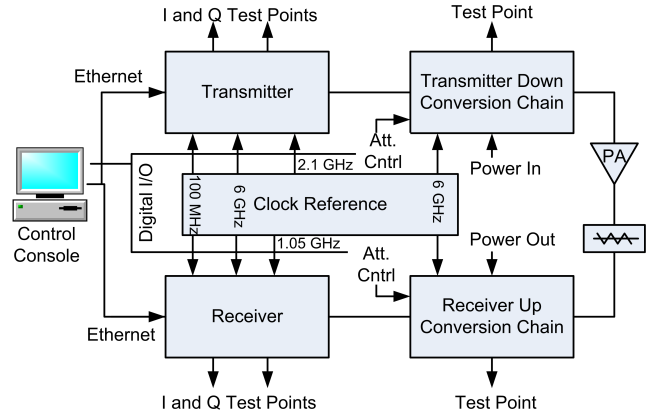


Fig. 5. Block diagram of CART's major components

MHz to 1750 MHz, amplify the signal to levels expected in fielded systems and then detect the transmitted signal for further processing. CART is composed of seven primary components: control console, transmitter, receiver, transmitting power amplifier, clock reference and two sets of converters.

All operations of the testbed are done through the control console using a custom design macro language developed in MATLAB. The language supports not only the testbed but all test instruments and sensors monitoring the experiment. First the waveform is loaded in the transmitter via the Ethernet interface. Through the Ethernet, GPIB and digital I/O card interfaces, the rest of the testbed is configured for operation. This includes setting the operating point on the transmitting amplifier, amplitude and phase equalization of the receiver, configuring the spectrum analyzers and power meters, and measuring system temperatures. Once the system is ready, the control console sends a trigger command to the transmitter to begin the experiment. In turn the transmitter responds with trigger pulses which synchronize the transmitter and receiver. This system may be scaled to support multiple transmitters and receivers to simulate multi-user environments.

An early concession in the CART design was to delay implementation of real-time processing. The significant effort required to implement operations in real-time fashion would have impeded the ability to efficiently test new processing manifold structures. As a result, all of the calculations for the synthesis of the waveform and post-processing are done off-line. Test waveforms are loaded into memory on the transmitter or retrieved from the receiver's memory via the control console. The FPGAs used in the transmitter and receiver have been sized to support real-time algorithms which may be implemented at a later date.

Using CART, communications waveforms (12-4 QAM) in 5 MHz of instantaneous bandwidth were transmitted at varying power levels occupying random center frequencies without overlap. An example of the comparative linearization performance of two 12-4 QAM waveforms synthesized from a single transmitter is illustrated in Fig. 6 after training with 12-4 QAM and band-limited AWGN waveforms at random center frequencies in 500 MHz of instantaneous bandwidth. Without digital compensation, two distortions that are 25-30 dBc down

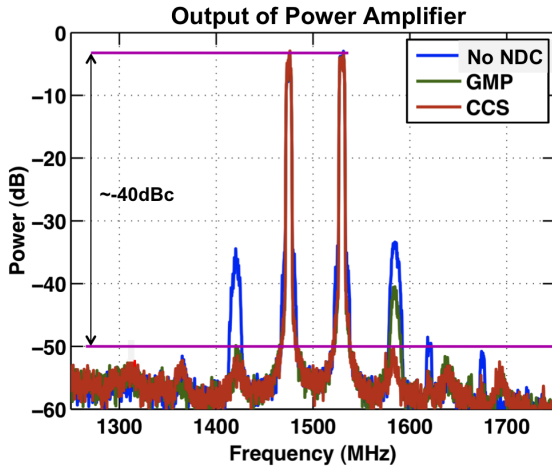


Fig. 6. An example of the comparative linearization performance of a two carrier 12-4 QAM waveform using GMP and CCS.

from the carrier straddle the two 12-4 QAM waveforms and represent the third order intermodulation product of the two spectrally segmented waveforms. There is also a loss in spectral containment of the 12-4 QAM waveforms due to spectral regrowth around each of the carriers. GMP was able to reduce the ACI by 6 dB. CCS, whose architecture was derived using sequential estimation with  $d = 2$ , was able to reduce ACI by roughly 15 dB pushing distortions virtually down to the noise floor, while containing spectral regrowth around each of the carriers.

A measure of the statistical performance of NDC is illustrated in Fig. 7. Three hundred different verification waveforms at random center frequencies were used to generate the measured cumulative distribution function of Fig. 7, where the  $y$ -axis represents the probability of ACI being no worse than the corresponding  $x$ -axis intercept. The objective spectral mask requirement was  $-35$  dBc representing a common joint tactical radio set (JTRS) [2] specification. The objective 99% likelihood of meeting spectral mask requirements is indicated by the dashed horizontal line. MP and GMP were able to achieve spectral masks of  $-26$  dBc and  $-32$  dBc; CCS was able to achieve a spectral mask of  $-36$  dBc with 99% likelihood. GMP and CCS NDC required roughly 250-300 operations per sample. MP had a lower operations per sample count but was unable to achieve ACI suppression better than  $-26$  dBc regardless of computational complexity.

Given the significant advantage in CR to transmit over non-contiguous frequencies, we measured the unintentional interference caused by such a transmitter on a communications signal occupying a distant frequency band. Fig. 8(a) shows that the two spectrally non-contiguous waveforms create a large distortion at 1300 MHz, which is reduced by an order of magnitude when CCS NDC is applied. Fig. 8(b) shows the same scenario with a neighboring communications waveform added at the distortion frequency. The signal-to-noise and distortion ratio (SINAD) of the communication receiver is significantly enhanced by using CCS NDP, and this has a great impact on demodulation performance. The EVM is improved

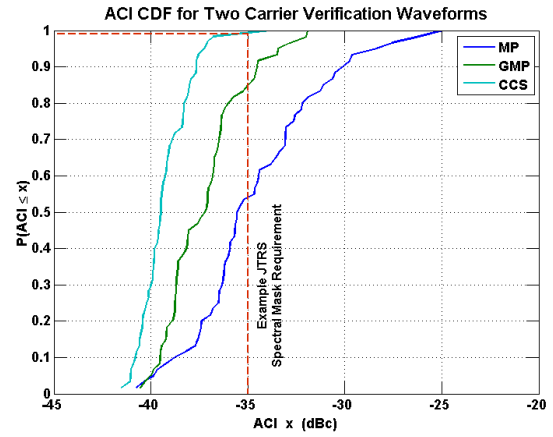
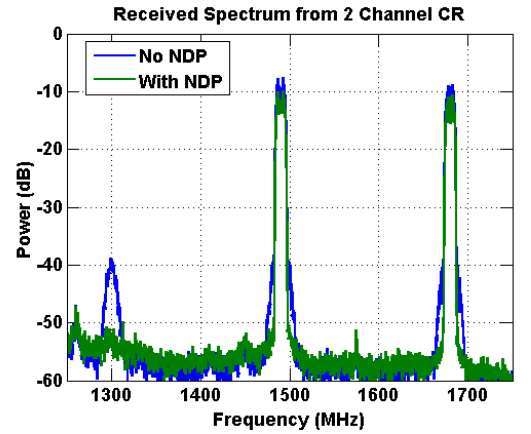
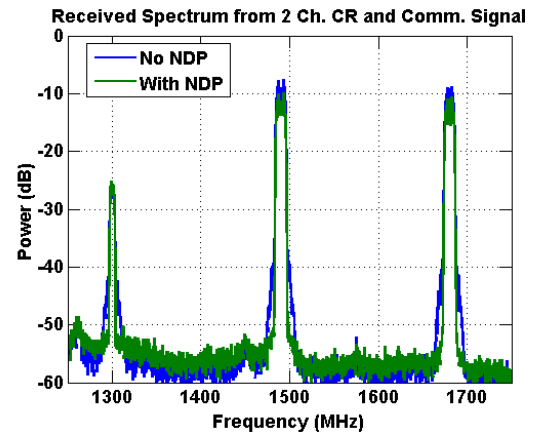


Fig. 7. Likelihood of being able to suppress ACI using MP, GMP and CCS.



(a)



(b)

Fig. 8. Two transmitters operating in the same 500 MHz band. A CR transmitting on two discontinuous frequencies generates both spectral regrowth and an out-of-band spur, shown in plot (a), and this interferes with a low-power neighboring communications signal, as shown in plot (b). Since nonlinear digital predistortion (NDP) pushes this distortion signal to the noise floor, the demodulated signal's EVM is improved by 13 dB.

by over 13 dB when CCS NDP is applied. Note that the small drop in amplitude of the main signal represents the elimination of distortions adding to each of the carriers. i.e., there was no input of output power backoff.



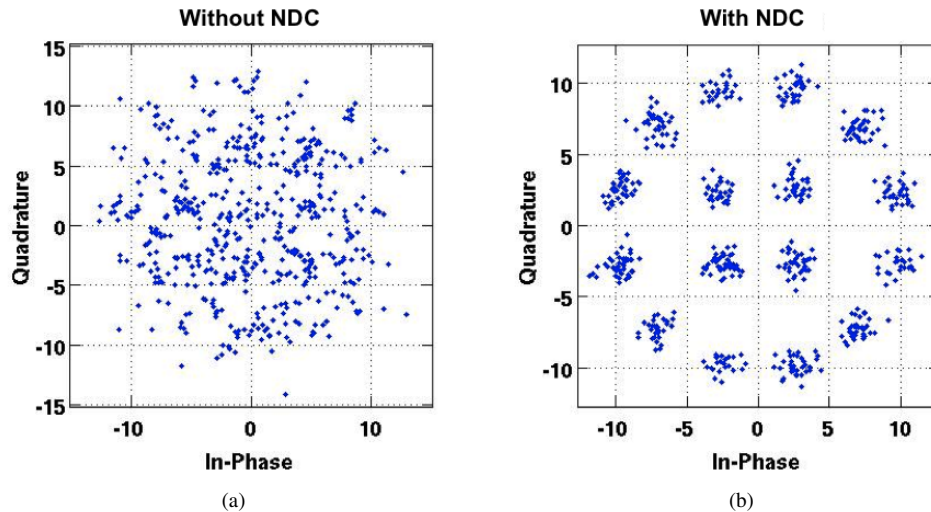


Fig. 9. I/Q scatter plot of a 12-4 QAM waveform at the receiver after digitization in the presence of very strong out-of-band interference. (a) Effect of receiver distortion on I/Q decision boundaries. (b) I/Q decision boundaries are clearly visible after receive CCS nonlinear digital compensation is applied.

We also applied the linearization algorithms to mitigate the distortions generated by the receiver on CART, where the receiver's dynamic range was limited principally by the high speed analog to digital converter. The measured effect of receiver distortion in a time-interleaved analog to digital converter on a 12-4 QAM waveform is illustrated in Fig. 9(a). One large out-of-band interferer generates distortions that land on top of the 12-4 QAM waveform. The uncompensated dynamic range of the receiver is roughly 50 dBFS, and the 12-4 QAM waveform is roughly 35 dB lower in power than the larger out-of-band signal. A polyphase extension of CCS nonlinear digital compensation (see [11]) extended the dynamic range of the receiver by almost two orders of magnitude. One tone dynamic range improved by 19 dB, and two and three tone dynamic range improved by 17 dB after polyphase NDC. The improvement in dynamic range enabled the recovery of the decision boundaries of the 12-4 QAM waveform clearly visible in Fig. 9(b).

#### IV. SUMMARY

In this paper we show that there is a clear advantage to wideband spectrally segmented operation for cognitive radio (CR) systems. A significant technical obstacle to deploying wideband spectrally segmented CR systems is the nonlinear response of both the receiver and transmitter. In this paper we present a novel approach to linearization of both the receiver and transmitter RF and mixed signal hardware. We develop a Cube Coordinate Subspace (CCS) architecture and optimization procedure for selecting CCS processing elements. We then demonstrate the linearization performance of CCS in CR scenarios, with results indicating CCS achieves nearly an order of magnitude improvement in linearization performance over current state-of-the-art approaches. Using measured results we demonstrate that CCS linearization makes wideband spectrally segmented CR a feasible choice for next generation communications systems. Future work will include extending the instantaneous bandwidth of CART to span 200 MHz

to 1900 MHz, and extending the linearization algorithm to efficiently operate over multiple octaves of bandwidth.

#### REFERENCES

- [1] G. Stabile and K. Webach, "The end of spectrum scarcity", *IEEE Spectrum*, 2004
- [2] B. Kimura, C. Carden and R. "North, Joint Tactical Radio System - empowering the warfighter for joint vision 2020". *Military Communications Conference*, San Diego, CA, 2008
- [3] T. Cover, J. Thomas, "Elements of Information Theory", *Wiley-Interscience*, 2006
- [4] J. Pedro and S. Maas, "A Comparative Overview of Microwave and Wireless Power-Amplifier Behavioral Modeling Approaches", *IEEE Transactions on Microwave Theory and Techniques*, vol. 53, pp. 1150-1163, 2005
- [5] R. Menon, R. Buehrer and J. Reed, "On the impact of dynamic spectrum sharing techniques on legacy radio systems", *IEEE Transactions on Wireless Communications*, vol. 7, pp. 4198-4207, 2008
- [6] S. Benedetto and E. Biglieri, *Principles of Digital Transmission with Wireless Applications*, Kluwer Academic, 1999.
- [7] M. Herman, B. Miller, and J. Goodman, "The cube coefficient subspace architecture for nonlinear digital predistortion," in *Proc. 42nd Asilomar Conference on Signals, Systems, and Computers*, 2008, pp. 1857-1861.
- [8] R. D. Nowak and Van Veen, B. D. "Random and pseudorandom inputs for Volterra filter", *IEEE Transactions on Signal Processing*, vol. 42, no. 8, pp. 2124-2135, 1994
- [9] N. Safari, P. Fedorenko, J. S. Kenney, and T. Roste "Spline-based model for digital predistortion of wideband signals for high power amplifier linearization," *IEEE MTT-S Int. Dig.*, p. 1441, Jun. 2007.
- [10] V. J. Mathews and G. L. Sicuranza, *Polynomial Signal Processing*, John Wiley & Sons, 2000.
- [11] J. Goodman, B. Miller, M. Heman et al., "Polyphase nonlinear equalization of time-interleaved analog-to-digital converters," *IEEE Journal of Selected Topics in Signal Processing*, vol. 3, pp. 362-373, June 2009.
- [12] J. Goodman, M. Herman, and B. Miller, "Cube coordinate subspaces for nonlinear digital predistortion," Patent Pending, 2007.
- [13] L. Ding, G. T. Zhou, D. R. Morgan, Z. Ma, J. S. Kenney, J. Kim, and C. R. Giardina, "A robust digital baseband predistorter constructed using memory polynomials," *IEEE Trans. Commun.*, vol. 52, no. 1, pp. 159-165, Jan. 2004.
- [14] D. R. Morgan, Z. Ma, J. Kim, M. G. Zierdt, and J. Pastalan, "A generalized memory polynomial model for digital predistortion of RF power amplifiers," *IEEE Trans. Signal Process.*, vol. 54, pp. 3852, Oct. 2006.
- [15] E. Candès and T. Tao, "The Dantzig selector: Statistical estimation when  $p$  is much larger than  $n$ ," *SIAM Annals of Statistics*, vol. 25, pp. 2313-2351, 2007.